Solar RRL
www.solar-rrl.com

Correlating Heteroatoms Doping, Electronic Structures, and Photocatalytic Activities of Single-Atom-Doped $Ag_{25}(SR)_{18}$ Nanoclusters

*Ye Liu, Deng Long, Andreas Springer, Rongbin Wang, Norbert Koch, Matthias Schwalbe, Nicola Pinna, and Yu Wang**

Atomic-level manipulation of catalysts is important for both fundamental studies and practical applications. Here, the central metal atom in an atomically precise Ag_{25} nanocluster (NC) is replaced with a single Pd, Pt, and Au atom, respectively, and employed as a model system to study the structure–property–activity relationship at the atomic level. While the geometric structures are well-preserved after doping, the electronic structures of Ag_{25} NCs are significantly altered. The combination of Ag_{25} and TiO_2 enhances the charge separation at the interface, exhibiting a 10 times higher hydrogen production rate in photocatalytic hydrogen evolution reaction compared to bare TiO_2. Further results show that heteroatoms doping has a negative impact on performance, particularly in the cases of Pd and Au doping. Ultraviolet photoelectron spectroscopy measurements and density functional theory calculations suggest that the lower activities are due to an energy mismatch between the levels of doped NCs and TiO_2. These findings not only reveal the impact of heteroatoms doping on the electronic properties and photocatalytic activities of NCs, but can also guide the design of heterometallic NCs for photocatalytic applications.

1. Introduction

Heterometallic nanoparticles have been emerging as a type of important nanomaterials exhibiting catalytic properties that are substantially different from their homometallic counterparts.[1–4] By altering the electronic structure or creating new active sites, the metal components in a heterometallic nanostructure often interplay with each other to induce synergetic effects.[5–9] Specifically, the synergetic effects are divided into ensemble effects and ligand effects.[10] Ensemble effects are geometrical effects due to the changes in the catalytic performances of an ensemble of atoms when the composition of the catalyst changes. Ligand effects refer to electronic effects due to changes in the chemical properties of the atoms due to the presence of multiple metal components.[10] In general, it is difficult to vary the composition of heterometallic nanoparticles without changing the electronic structure of the individual metal components and affecting the metal distribution.[11] Several techniques like atom probe tomography and low-energy ion scattering spectroscopy have been used for the characterization of metal distributions in heterometallic nanoparticles.[3,9] However, the characterization of metal distribution at the atomic scale remains challenging.

Metal nanoclusters (NCs) with atomic precision are a unique family of metal nanomaterials that are readily crystallized into single crystals, representing ideal models to unravel structure–property relationship at the atomic level.[12–14] By tuning the number of metal atoms in the core, the composition, and the protecting ligand of metal NCs, their physicochemical properties can be precisely controlled.[15,16] Taking the well-studied Au NCs as an example, their ground state and excited state electronic structures are tunable. The photoluminescence quantum yield of a rod-shaped Au_{25} NC can be tuned from 0.1% to 40.1% by substituting gold atoms with silver.[17] The lifetime of the excited charge carriers of gold NCs can be as long as 5 μs depending on the structures.[18]

Y. Liu, D. Long, R. Wang, M. Schwalbe, N. Pinna, Y. Wang
Department of Chemistry and IRIS Adlershof
Humboldt-Universität zu Berlin
12489 Berlin, Germany
E-mail: wangyuxx@hu-berlin.de

The ORCID identification number(s) for the author(s) of this article can be found under https://doi.org/10.1002/solr.202201057.

© 2023 The Authors. Solar RRL published by Wiley-VCH GmbH. This is an open access article under the terms of the Creative Commons Attribution-NonCommercial-NoDerivs License, which permits use and distribution in any medium, provided the original work is properly cited, the use is non-commercial and no modifications or adaptations are made.

DOI: 10.1002/solr.202201057

D. Long
Pen-Tung Sah Institute of Micro-Nano Science and Technology
Xiamen University
Xiamen 361005, China

A. Springer
Core Facility BioSupraMol
Institute of Chemistry and Biochemistry
Department of Biology, Chemistry and Pharmacy
Freie Universität Berlin
14195 Berlin, Germany

R. Wang, N. Koch
Department of Physics and IRIS Adlershof
Humboldt-Universität zu Berlin
12489 Berlin, Germany

Zhu et al reported that a subtle alteration of silver NCs by central doping with a foreign atom dramatically changed the catalytic performance of the NCs for CO_2 conversion.[19] Zheng et al. reported that the protecting ligands of the NCs play an important role in the hydrolytic oxidation of organosilanes since the ligands were involved in the formation of reaction intermediates.[20]

Recently, the utilization of metal NCs in photocatalytic and photoelectrochemical reactions has been emerging as a new field and gained significant attention.[21–27] The strong, broad light absorption ability and the long-lived excited states make metal NCs promising candidates as photosensitizer, and might replace traditional dyes.[18,28–31] Their discrete energy levels allow them to prevent charge recombination at the semiconductor by efficiently separating the photoinduced charge carriers.[32] Moreover, these metal NCs themselves can act as active catalysts.[33–35] By replacing the protecting ligands of an undecagold NC from triphenylphosphine to diphenylphosphine oxide, the functionalized Au_{11}/Bi_2O_3 composite showed high selectivity toward the hydrogenation of the C = O group in benzaldehyde.[36] Compared to the size effects of metal NCs on the photocatalytic/photoelectrochemical performance, studies focusing on the doping effects, especially with a clear distinction between geometrical effects and electronic effects, are rare.[15,37–43]

Herein, $Ag_{25}(SR)_{18}$ NCs (SR = thiolate) are chosen as model catalysts to investigate the role of doping on the photocatalytic properties, where heteroatoms (e.g., Pd, Pt, and Au) replace the central Ag atom in Ag_{25} NCs. Since the main structure of Ag_{25} remains unchanged after central doping, the geometrical effects and the electronic effects can be clearly distinguished. The photocatalytic activities of as-prepared NCs deposited onto TiO_2 are investigated. The MAg_{24}/TiO_2(M = Ag, Pd, Pt, and Au) composite photocatalysts exhibit up to 10 times higher hydrogen production rate in photocatalytic hydrogen evolution reaction (HER) compared to bare TiO_2. However, the heteroatoms doping deteriorates the catalytic activities of the silver NCs. Density functional theory (DFT) calculations are performed to analyze the impact of heteroatoms doping on the electronic structures of the NCs, and UPS measurements are utilized to analyze the charge transfer pathways of the catalysts. The deterioration of the photocatalytic activities is attributed to a mismatch in energy levels between the doped NCs and TiO_2.

2. Results and Discussion

The five NCs protected by 2,4-Dimethylbenzenethiol were prepared by the methods reported previously.[19,44] The schematic overview of the structures of the NCs is shown in **Figure 1**a. Since Au, Pt, and Pd have higher cohesive energy than Ag, the dopant atoms prefer to occupy the high-coordinated site (center of the icosahedra Ag_{12}) in Ag_{25} NCs.[44] All the samples were characterized by mass spectrometry and UV–vis absorption spectroscopy. As determined by the electrospray ionization mass spectrometry (Figure 1b, see also Supporting Information), the signals at m/z 5165.4, 2582.2, 2626.2, and 5255.5 could be assigned as Ag_{25}, $PdAg_{24}$, $PtAg_{24}$, and $AuAg_{24}$, respectively. All the experimental results correspond well with the simulated results, confirming the atomic compositions of the NCs. UV–vis absorption spectra in Figure 1c showed the different absorption profiles of MAg_{24} NCs, where significant blue shifts were observed for the heteroatoms doped MAg_{24} NCs. To correlate the structure parameters to the optical properties of the NCs, density functional theory (DFT) calculations were performed. Taking the adsorption spectra of Ag_{25} NCs as an example, the adsorption bands at around 677 and 488 nm correspond to the LUMO + 1 ← HOMO transition (α) and LUMO + 2 ← HOMO-2 (β) transition, which are essentially intraband (sp ← sp) transitions. However, when the heteroatoms are incorporated into the core of the MAg_{24} NCs, these transitions arise essentially from interband (sp ← d) transitions, indicating the perturbation of the electronic structures induced by the heteroatoms.[45] The transition behaviors for Ag_{25}, $PdAg_{24}$, and $AuAg_{24}$ NCs are identical, however, the β transition of $PtAg_{24}$ NCs exhibit different transition behaviors, which originate from HOMO-2 orbital to high-lying LUMO + 4 orbital.

It has been experimentally verified that the core of the Ag_{25} NCs is made up of an Ag_{12} icosahedral core with one Ag atom situated at its center. The remaining 12 Ag atoms form six $Ag_2(SR)_3$ dimeric staples and occupy the 12 triangular faces of the $Ag@Ag_{12}$ icosahedron, forming a core–shell structure.[44] The electronic structures of the as-prepared NCs were also analyzed based on the DFT calculations, **Figure 2** shows the Kohn–Sham (KS) orbitals of MAg_{24} NCs with the contribution of each valence orbital component marked in different colors. The highest occupied molecular orbital (HOMOs) and lowest unoccupied molecular orbital (LUMOs) of the four NCs are mainly contributed by Ag(4d) and Ag(sp) orbitals, with the former contributing more in the LUMOs, whereas the latter have stronger contribution in the HOMOs. The participation of Ag(sp) and M(sp) orbitals in the $PtAg_{24}$ NCs is obviously less pronounced than that in $PdAg_{24}$ and $AuAg_{24}$ NCs, this result is in accordance with the relatively shorter M-Ag bond lengths among the doped NCs (**Table 1**).[46] A similar phenomenon could also be found in the LUMOs of the NCs, the contribution of Pt(5d) is less pronounced than the other two doped NCs, which indicates weaker d–d hybridization between Pt and the Ag atoms in $PtAg_{24}$ NCs. Ag_{25}, $PdAg_{24}$, and $AuAg_{24}$ exhibit similar band structures with closed HOMO and LUMO positions. However, $PtAg_{24}$ shows dramatically decreased HOMO and LUMO positions compared to the other NCs, with the positions being −3.12 and −2.48 eV, respectively.

There are mainly three excited-state species included in MAg_{24} NCs: 1) the higher excited-states; 2) surface-states; 3) a state consisting of low-lying LUMOs centered on the metal core.[46,47] According to the energy evolution and the above-mentioned relaxation process, the MAg_{24} NCs could be readily sorted into two types—type A ($PtAg_{24}$) and type B (Ag_{25}, $PdAg_{24}$, and $AuAg_{24}$), where the orbital coupling is stronger between LUMO + 1 and the other high-lying LUMOs in type B. Compared to type B NCs, type A NCs present narrower HOMO–LUMO gaps and wider energy gap between LUMO + 1 and the other high-lying LUMO orbitals, which leads to slower electron relaxation from high exited-states to low-lying LUMO orbitals.[48] Moreover, due to the faster loss of quantum coherence, type A NCs exhibit stronger electron-vibration interactions and elastic scattering upon heteroatoms doping, which further prolongs the electron relaxation time.[49,50]

The direct visualization of the HOMOs and LUMOs is presented in the insets of Figure 2. The frontier orbitals

© 2023 The Authors. Solar RRL published by Wiley-VCH GmbH

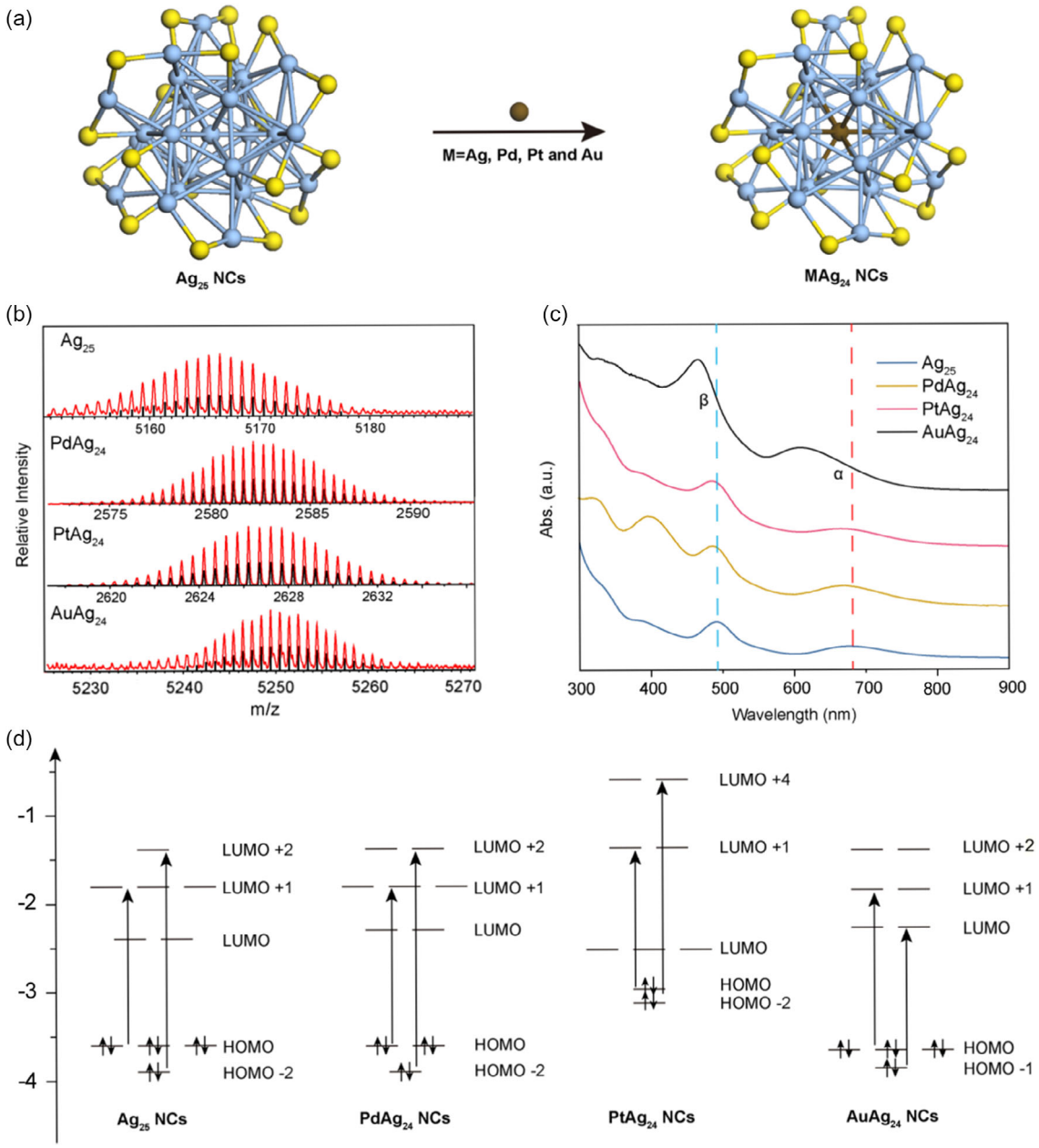

Figure 1. a) Schematic illustration of the structure of MAg_{24} nanoclusters (NCs). b) Simulated (Black) and experimental (Red) electrospray ionization mass spectrometry (ESI-MS) spectra of the as-prepared NCs. c) UV–Vis absorption spectra of the as-prepared NCs. d) Electronic energy levels of the NCs.

match well with the characteristics of the superatom concept, where the doubly degenerate LUMO of Ag_{25} and HOMO of $PdAg_{24}$ NCs present superatomic d-type and p-type orbitals (Figure 1d and top part of Figure 2), respectively.[51] However, the cases are different for $PtAg_{24}$ due to a larger effective number of valence electrons participating in alloying. The electrons in singly degenerate HOMO are delocalized further away from the central Pt atoms in $PtAg_{24}$ NCs than that in other NCs, while the triply degenerate LUMO is rather localized (Figure 1d and bottom left of Figure 2). Interestingly, $PtAg_{24}$ exhibit d-type HOMO and p-type LUMO which is different from the other three NCs. For $AuAg_{24}$ NCs, the triply degenerate HOMO shows superatomic p-type orbitals and the doubly degenerate LUMO shows d-type orbitals (Figure 1d and bottom right of Figure 2).

To analyze the charge distribution across the scaffold of the NCs, charge density contour plots were mapped from the *Z*-axis (**Figure 3**a). The charge density surrounding the core atoms is much higher than the ligands in all the NCs, this phenomenon is more evident in Ag_{25} and $PtAg_{24}$ than in the other doped NCs. The stronger charge density in the metal cores would polarize the metal atoms and orbitals to form a permanent internal electric field (IEF) within the core, thus driving the electrons and holes to the metal core and ligands, respectively.[52–54] The heteroatom

© 2023 The Authors. Solar RRL published by Wiley-VCH GmbH

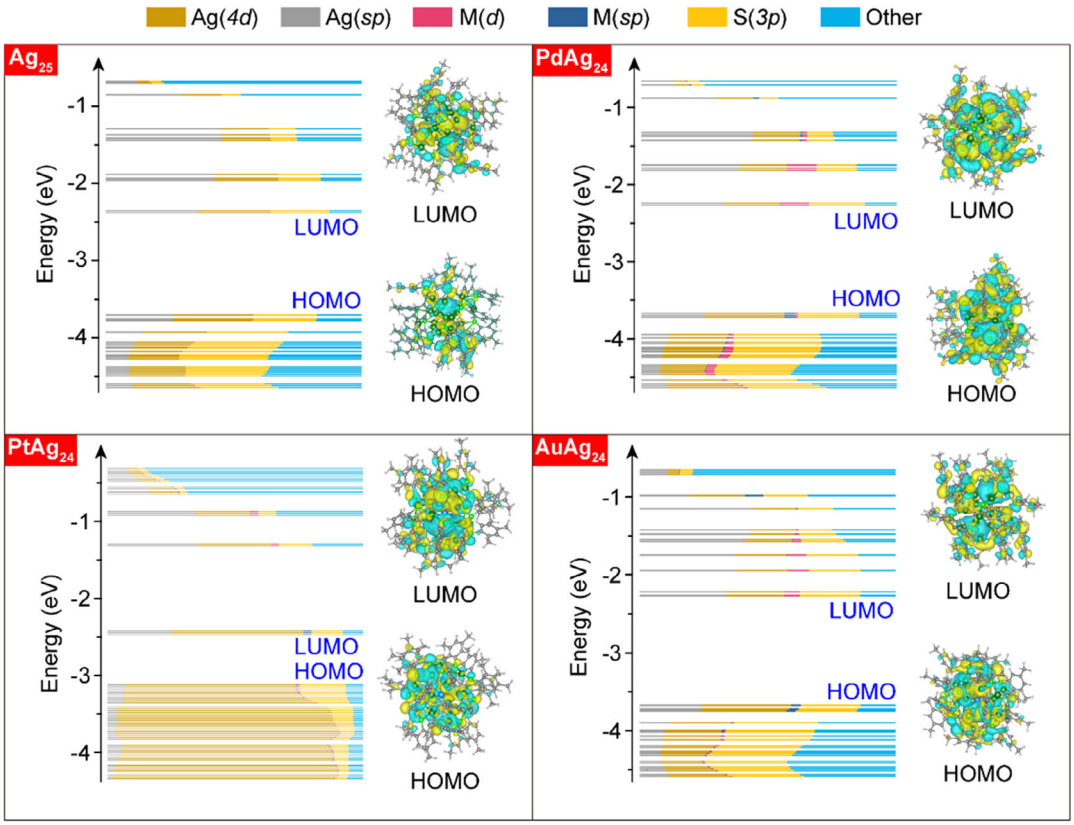

Figure 2. Kohn–Sham (KS) orbitals and visualized HOMO and LUMO orbitals of MAg_{24} NCs obtained from density functional theory (DFT) calculations. The different colors in the energy levels show the contribution of the stated atomic orbitals.

Table 1. The positions of the energy levels of MAg_{24} NCs and the average *M*-Ag ($d_{M\text{-Ag}}$) bond lengths of the NCs at the lowest energy.

NCs	HOMO[a]	LUMO	LUMO + 1	E_{Fermi}	E_{HL}	E_{L+1}	$d_{M\text{-Ag}}$(Å)
Ag_{25}	−3.70	−2.37	−1.95	−3.66	1.33	0.42	2.764
$PdAg_{24}$	−3.67	−2.26	−1.82	−3.65	1.40	0.44	2.754
$PtAg_{24}$	−3.12	−2.48	−1.30	−3.30	0.64	1.18	2.750
$AuAg_{24}$	−3.68	−2.26	−1.93	−3.64	1.42	0.33	2.774

[a]E_{Fermi}, position of the Fermi level; E_{HL}, energy difference between HOMO and LUMO; E_{L+1}, energy difference between LUMO + 1 and LUMO; $d_{M\text{-Ag}}$, the distance between the core metal atoms and the Ag atoms at the inner shell.

doping also takes effect in the adsorption behaviors of the NCs, where the adsorption peaks of the doped MAg_{24} NCs are more significantly blue-shifted than the Ag_{25} NC. Other features could also be observed in the density of states (DOS) of MAg_{24} NCs: heteroatoms doping degenerates the electronic states and induces the impurity levels in the pseudo gap impurity levels (Figure S1, Supporting Information).[55]

Photocatalytic H_2 evolution reaction was selected as a model reaction to investigate the impact of the heteroatoms doping on the catalytic activities. The as-prepared NCs were loaded onto TiO_2 and used as catalysts. For clarification, they were named as Ag_{25}/TiO_2, $PdAg_{24}/TiO_2$, $PtAg_{24}/TiO_2$, and $AuAg_{24}/TiO_2$, respectively. All the samples were measured under UV–vis light illumination. As is shown in Figure 3b, a trace amount of hydrogen was detected on the pristine TiO_2 catalyst after 18 h of illumination, which is 9.80 μmol $g_{catal.}^{-1}\,h^{-1}$. Notably, the composite Ag_{25}/TiO_2 catalysts exhibited a much higher HER rate than the bare TiO_2 (102.94 μmol $g_{catal.}^{-1}\,h^{-1}$). We also measured the HER rates for the doped MAg_{24}/TiO_2 catalysts to investigate the impact of heteroatoms doping on the catalytic activities. All the doped MAg_{24}/TiO_2 catalysts still exhibit better performance than the bare TiO_2. However, there are deteriorations in the catalytic activities after Pd or Au doping compared to the undoped Ag_{25}/TiO_2 catalyst.

The performance of the MAg_{24} NCs were 74.08, 37.89, 71.13, and 37.14 mmol $g_{NCs}^{-1}\,h^{-1}$ for Ag_{25}, $PdAg_{24}$, $PtAg_{24}$, and $AuAg_{24}$ NCs, respectively (Figure 3c). To further investigate the charge dynamics and the structure–activity relationships of MAg_{24} NCs, the energy band alignments of the MAg_{24}/TiO_2 composite catalysts were investigated by X-Ray photoelectron spectroscopy (XPS) and UPS. Obvious shifts toward lower binding energy of ≈0.15 eV could be observed upon the deposition of MAg_{24} NCs, indicating an upward band bending (Figure 3d). The valence band maximum (VBM) of TiO_2 was located at 3.20 eV below the Fermi level according to the UPS spectra (Figure 3e), while the HOMO of Ag_{25} NCs was found to be at ≈1.26 eV (Figure S2, Supporting Information). Thus, the conduction band minimum (CBM)

© 2023 The Authors. Solar RRL published by Wiley-VCH GmbH

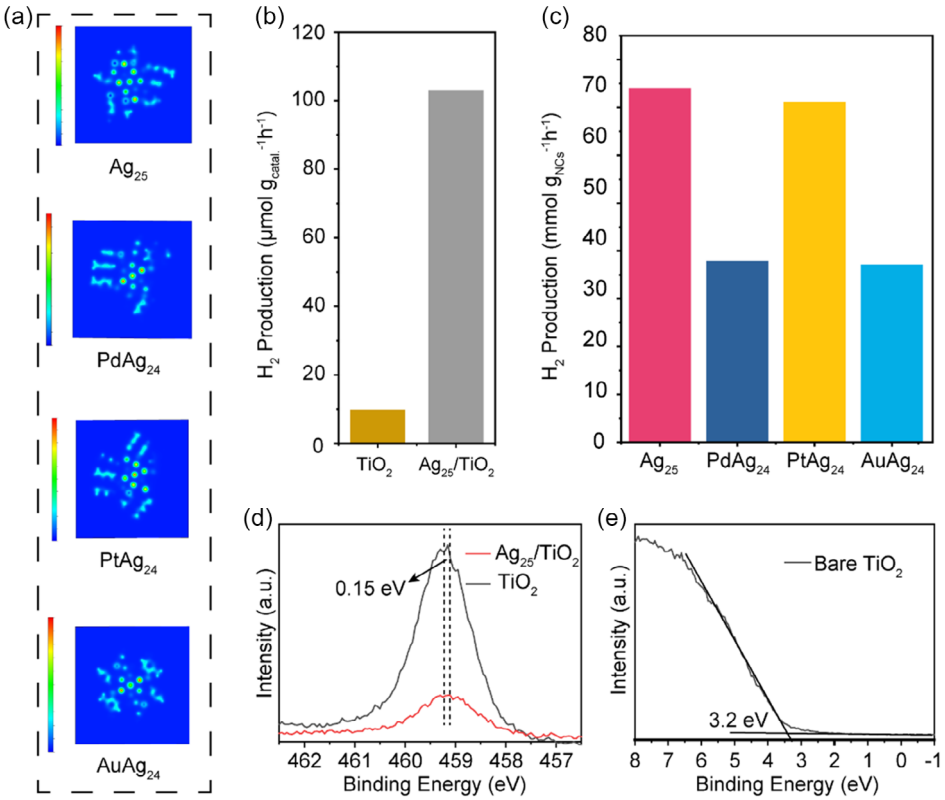

Figure 3. a) Charge density plots of MAg_{24} NCs mapped from the Z-axis. b) Hydrogen evolution reaction (HER) rates of bare TiO_2 and Ag_{25}/TiO_2 catalysts. c) HER rates correlated by NCs. d) The shift of Ti $2p_{3/2}$ of bare TiO_2 and Ag_{25}/TiO_2. e) Valence band X-Ray photoelectron spectroscopy (XPS) spectrum of pristine TiO_2.

and LUMOs could be determined according to the values of HOMO–LUMO gaps (Table 1).[32,56]

Based on the results obtained earlier, the energy diagram of the Ag_{25}/TiO_2 composite catalyst could be deduced (**Figure 4**a). Upon the contact of Ag_{25} NCs, a band bending occurred on the surface band of TiO_2 and the Fermi levels align, leading to a change in the near-surface space-charge region.[57] While the LUMO of Ag_{25} NC is lower than the CBM of TiO_2, the LUMO + 1 is higher than the CBM. When the Ag_{25}/TiO_2 catalyst is illuminated, a staggered Type II charge transfer scheme with high charge separation efficiency is formed: the photoinduced electrons in the LUMO + 1 or higher energy states of the NC are transferred to the CB of TiO_2 for reduction reaction, while the photoinduced holes from TiO_2 are transferred to the HOMO of the NC for the oxidation reaction.[58,59] Since the main absorption band at 677 nm corresponds to the LUMO + 1 ← HOMO transition, the role of LUMO + 1 in the charge transfer process is important (Figure 1d). Moreover, the LUMO + 1 orbital of Ag_{25} NCs exhibits diffuse superatomic d-type orbitals, where strong hybridization would occur among the interfacial atoms and thus facilitate the transfer of photoinduced electrons in space, further contributing to the electron–hole pairs separation.[46] Therefore, it could be concluded that the improved charge separation in Ag_{25}/TiO_2 leads to greatly enhanced photocatalytic activities compared to the bare TiO_2.

To elucidate the impact of heteroatoms doping on photocatalytic activities, the energy-level diagrams of the other composites were also studied. Since the LUMO of $PtAg_{24}$ NC is lower than the CBM of TiO_2, the charge transfer in $PtAg_{24}/TiO_2$ follows a similar process as Ag_{25}/TiO_2 (Figure 4c). Electrons that are excited to the LUMO are not involved in the interfacial charge transfer. Instead, the prolonged electron relaxation time in $PtAg_{24}$ allows for reactions between the photoinduced electrons in LUMO and the protons adsorbed on the NCs. This partially accounts for the best performance of $PtAg_{24}/TiO_2$ among doped samples. The cases for $PdAg_{24}/TiO_2$ and $AuAg_{24}/TiO_2$ catalysts are different. As is shown in Figure 4b,d, the LUMO positions of $PdAg_{24}$ and $AuAg_{24}$ NCs are both above the CBM of TiO_2, indicating that the electrons that are excited to the LUMO of the NCs will also transfer to the CB of TiO_2. The charge density contour plots in Figure 3a provide further evidence of the difference in the catalytic HER rates of the catalysts. It is known that the metal sites of NCs are recognized as the active sites for H^+ reduction into molecular H_2, the relatively lower charge density in the core metal atoms of $PdAg_{24}$ and $AuAg_{24}$ NCs make them less favorable for hydrogen evolution compared to the Ag_{25} and $PtAg_{24}$ NCs.[60]

3. Conclusion

In conclusion, we investigated the impact of single heteroatom (Pd, Pt, and Au) doping on the electronic structures and photocatalytic activities of Ag_{25} NCs. While the geometric structures

© 2023 The Authors. Solar RRL published by Wiley-VCH GmbH

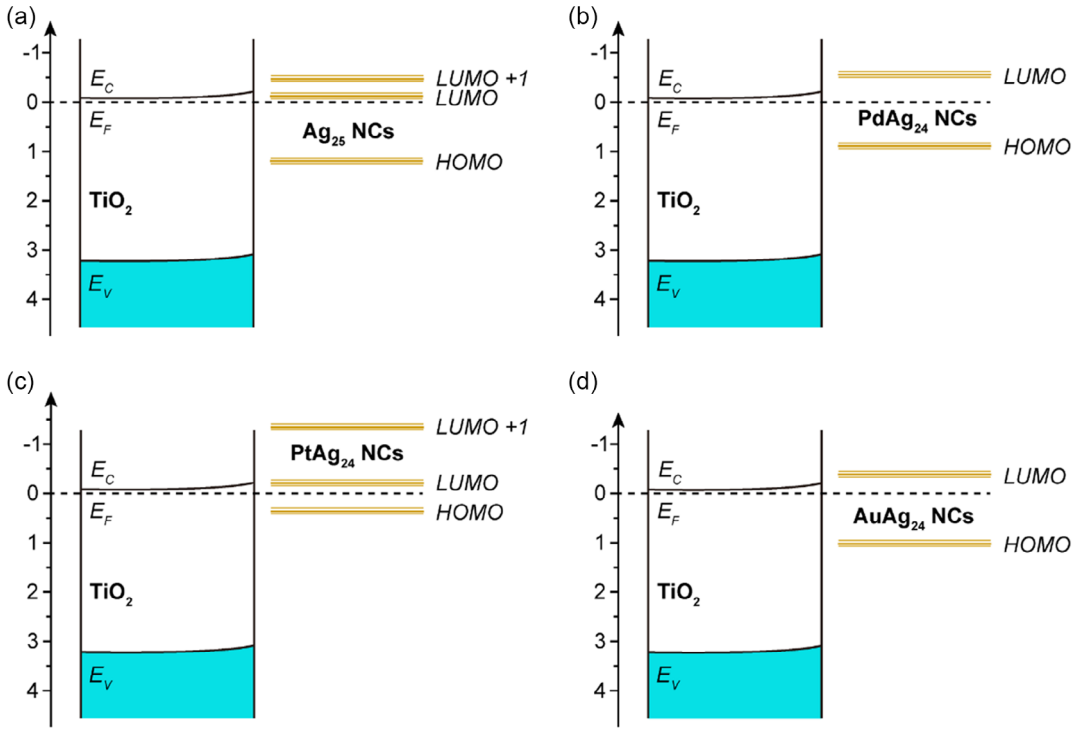

Figure 4. Schematic energy level diagrams of a) Ag_{25}/TiO_2, b) $PdAg_{24}/TiO_2$, c) $PtAg_{24}/TiO_2$, and d) $AuAg_{24}/TiO_2$ composite catalysts, respectively.

are well-preserved after doping, the electronic structures of Ag_{25} NCs were significantly altered. The combination of Ag_{25} and TiO_2 enhanced the charge separation at the interface, exhibiting a 10 times higher hydrogen production rate in the photocatalytic HER compared to bare TiO_2. Further results showed that heteroatoms doping deteriorated the catalytic activities of the NCs, following the order of $Ag_{25} \geq PtAg_{24} > PdAg_{24} \geq AuAg_{24}$. UPS measurements and DFT calculations allowed to conclude that the lower activities are mainly due to the mismatch in energy levels between the doped NCs and TiO_2. These findings not only reveal the impact of heteroatoms doping on the electronic structure and photocatalytic activities of NCs, but also suggest an important criterion for the design of heterometallic NCs for photocatalytic applications. We hope that this study will stimulate more studies focusing on the band alignment between metal NCs and the targeted support while tuning the electronic structures of the desired metal NCs, in which way the charge transfer is facilitated and the utilization of solar energy is improved.

4. Experimental Section

Synthesis of MAg_{24} NCs: All the NCs were synthesized according to the reported reference without any further modifications.[19,44]

Synthesis of MAg_{24}/TiO_2 Catalysts: 0.5 g of commercial anatase TiO_2 powder was first dispersed in 5 mL of dichloromethane. Then 6 wt% equivalent amount of NCs solids was added into the mixture, which was further allowed to be stirred under ambient conditions until the adsorption equilibrium had been reached.

Photoelectron Spectroscopy Characterization: The characterization of the bare TiO_2 and MAg_{24}/TiO_2 was performed using UPS and X-Ray photoelectron spectroscopy (XPS) with a hemispherical electron analyzer (PHOIBOS-100, SPECS) using a the non-monochromated Al Kα (1486.6 eV) radiation of a dual anode X-ray source (SPECS XR 50) and a monochromated HeIα (21.22 eV) discharge lamp (Scienta Omicron HIS13 combined with a VUV5K monochromator). A − 10 V bias voltage was applied during the measurement of the secondary electron cutoff (SECO). All measurements were performed at room temperature. All energies are referred to as the Fermi-level (EF).

Mass Spectrometry: The samples were analyzed with a Synapt G2-S HDMS mass spectrometer, Waters Co., USA. The ionization and transfer conditions of the mass spectrometer were optimized for the maximal intensity of the cluster (Ag_{25} NCs) and used unchanged for all other samples. Negative ESI-MS with a capillary voltage of 1.46 kV was used. The source temperature was set to 40 °C, the desolvation temperature was set to 120 °C. The sampling cone and source offset voltages were set to 25 and 40 V. The desolvation gas flow was 400.0 L hr^{-1}. IMS Bias and Trap DC Bias were lowered to 1.5 V. All Measurements have been performed in resolution mode ($R \approx 25\,000$). Initial calibration for m/z 400 to 8000 was performed utilizing a 2 mg mL^{-1} CsI solution (CsI: analytical standard for high-resolution mass spectrometry, Fluka, CH, Solvents: 3:1 ULC/MS-grade 2-Propanol: ULC/MS-grade water, purchased at BioSolve BV, NE). LockSpray (ESI-L low concentration Tuning Mix, Agilent Technologies, USA, diluted 1:10 with ULC/MS grade ACN, with peaks at m/z 1033.9881 and m/z 2833.8731) was used throughout the experiments to improve mass accuracy. All samples have been dissolved in Dichloromethane (stabilized with Ethanol, HPLC grade).

DFT Calculations: All calculations were performed using the first-principles DFT with the exchange-correlation energy function of the generalized gradient approximation (GGA) by adopting the Perdew–Burke–Ernzerhof (PBE). The calculations were conducted by using the VASP package, in which the ultrasoft pseudopotentials were employed for all atoms with the accuracy set as Accurate. The cluster was put in a $30 \times 30 \times 30$ Å^3 cubic box, and the initial structure of the cluster was from the crystallographic information file provided by the reported references. All the ligands and hydrogen atoms were included in the models and were well-relaxed via geometry optimization before the energy

© 2023 The Authors. Solar RRL published by Wiley-VCH GmbH

calculations. An energy cutoff of 400 eV and a Monkhorst–Pack grid with a $1 \times 1 \times 1$ K-point set were chosen for the calculations. All the calculated data were post-processed with the VASPKIT package.

Supporting Information

Supporting Information is available from the Wiley Online Library or from the author.

Acknowledgements

The authors thank the German Research Foundation (DFG, Project 456075917 and 182087777-SFB951) for the financial support of this work. Y.L. and L.D. acknowledge financial support from China Scholarship Council (CSC, No. 201908420279 and No. 202106310045). The authors would also like to acknowledge the assistance of the Core Facility "BioSupraMol," Freie Universität Berlin, supported by the DFG.

Conflict of Interest

The authors declare no conflict of interest.

Data Availability Statement

The data that support the findings of this study are available from the corresponding author upon reasonable request.

Keywords

atomic precision, doping, metal nanoclusters

Received: November 25, 2022
Revised: December 28, 2022
Published online: January 15, 2023

[1] D. Wang, Y. Li, *Adv. Mater.* **2011**, *23*, 1044.
[2] B. Wu, N. Zheng, *Nano Today* **2013**, *8*, 168.
[3] R. Ferrando, J. Jellinek, R. L. Johnston, *Chem. Rev.* **2008**, *108*, 845.
[4] D. Chen, Y. Wang, D. Liu, H. Liu, C. Qian, H. He, J. Yang, *Carbon Energy* **2020**, *2*, 443.
[5] J. W. Hong, D. Kim, Y. W. Lee, M. Kim, S. W. Kang, S. W. Han, *Angew. Chem., Int. Ed.* **2011**, *50*, 8876.
[6] A. U. Nilekar, S. Alayoglu, B. Eichhorn, M. Mavrikakis, *J. Am. Chem. Soc.* **2010**, *132*, 7418.
[7] S. Alayoglu, A. U. Nilekar, M. Mavrikakis, B. Eichhorn, *Nat. Mater.* **2008**, *7*, 333.
[8] S. Alayoglu, B. Eichhorn, *J. Am. Chem. Soc.* **2008**, *130*, 17479.
[9] K. Tedsree, T. Li, S. Jones, C. W. A. Chan, K. M. K. Yu, P. A. J. Bagot, E. A. Marquis, G. D. W. Smith, S. C. E. Tsang, *Nat. Nanotech.* **2011**, *6*, 302.
[10] P. Liu, J. K. Nørskov, *Phys. Chem. Chem. Phys.* **2001**, *3*, 3814.
[11] R. W. Judd, M. A. Reichelt, R. M. Lambert, *Surf. Sci.* **1988**, *198*, 26.
[12] I. Chakraborty, T. Pradeep, *Chem. Rev.* **2017**, *117*, 8208.
[13] Y. Yang, T. Jia, Y.-Z. Han, Z.-A. Nan, S.-F. Yuan, F.-L. Yang, D. Sun, *Angew. Chem., Int. Ed.* **2019**, *58*, 12280.
[14] B. Han, Z. Wang, R. Gupta, L. Feng, S. Wang, M. Kurmoo, Z. Gao, S. Schein, C. Tung, D. Sun, *ACS Nano* **2021**, *15*, 8733.
[15] C. M. Aikens, *Acc. Chem. Res.* **2018**, *51*, 3065.
[16] Z. Wang, R. Senanayake, M. C. Aikens, W. Chen, C. Tung, D. Sun, *Nanoscale* **2016**, *8*, 18905.
[17] S. Wang, X. Meng, A. Das, T. Li, Y. Song, T. Cao, X. Zhu, M. Zhu, R. Jin, *Angew. Chem., Int. Ed.* **2014**, *53*, 2376.
[18] M. Zhou, T. Higaki, G. Hu, M. Y. Sfeir, Y. Chen, D.-E. Jiang, R. Jin, *Science* **2019**, *364*, 279.
[19] Y. Liu, X. Chai, X. Cai, M. Chen, R. Jin, W. Ding, Y. Zhu, *Angew. Chem., Int. Ed.* **2018**, *57*, 9775.
[20] Y. Wang, X.-K. Wan, L. Ren, H. Su, G. Li, S. Malola, S. Lin, Z. Tang, H. Häkkinen, B. K. Teo, Q.-M. Wang, N. Zheng, *J. Am. Chem. Soc.* **2016**, *138*, 3278.
[21] F.-X. Xiao, S.-F. Hung, J. Miao, H.-Y. Wang, H. Yang, B. Liu, *Small* **2015**, *11*, 554.
[22] N. Sakai, T. Tatsuma, *Adv. Mater.* **2010**, *22*, 3185.
[23] C. Yu, G. Li, S. Kumar, H. Kawasaki, R. Jin, *J. Phys. Chem. Lett.* **2013**, *4*, 2847.
[24] Y.-S. Chen, P. V. Kamat, *J. Am. Chem. Soc.* **2014**, *136*, 6075.
[25] M. A. Abbas, P. V. Kamat, J. H. Bang, *ACS Energy Lett.* **2018**, *3*, 840.
[26] R. Khan, M. H. Naveen, J. H. Bang, *ACS Energy Lett.* **2021**, *6*, 2713.
[27] Y. Liu, E. Wierzbicka, A. Springer, N. Pinna, Y. Wang, *J. Phys. Chem. C* **2022**, *126*, 1778.
[28] S. Hossain, D. Hirayama, A. Ikeda, M. Ishimi, S. Funaki, A. Samanta, T. Kawawaki, Y. Negishi, *Aggregate* **2022**, e255.
[29] T. Chen, H. Lin, Y. Cao, Q. Yao, J. Xie, *Adv. Mater.* **2022**, *34*, 2103918.
[30] Y. Wang, X.-H. Liu, S. A. Kovalenko, Q.-Y. Chen, N. Pinna, *Euro. J. Chem.* **2019**, *25*, 4814.
[31] M. Pelton, Y. Tang, O. M. Bakr, F. Stellacci, *J. Am. Chem. Soc.* **2012**, *134*, 11856.
[32] Y. Wang, X. H. Liu, Q. Wang, M. Quick, S. A. Kovalenko, Q. Y. Chen, N. Koch, N. Pinna, *Angew. Chem., Int. Ed.* **2020**, *59*, 7748.
[33] J. Yan, B. K. Teo, N. Zheng, *Acc. Chem. Res.* **2018**, *51*, 3084.
[34] Y. Negishi, *Bull. Chem. Soc. Jpn.* **2014**, *87*, 375.
[35] Q. Yao, Z. Wu, Z. Liu, Y. Lin, X. Yuan, J. Xie, *Chem. Sci.* **2021**, *12*, 99.
[36] Y. Wang, X.-H. Liu, R. Wang, B. Cula, Z.-N. Chen, Q. Chen, N. Koch, N. Pinna, *J. Am. Chem. Soc.* **2021**, *143*, 9595.
[37] K. L. D. M. Weerawardene, C. M. Aikens, *J. Phys. Chem. C* **2018**, *122*, 2440.
[38] M. H. Naveen, R. Khan, M. A. Abbas, E. Cho, G. J. Lee, H. Kim, E. Sim, J. H. Bang, *Chem. Sci.* **2020**, *11*, 6248.
[39] S. Hossain, Y. Niihori, L. V. Nair, B. Kumar, W. Kurashige, Y. Negishi, *Acc. Chem. Res.* **2018**, *51*, 3114.
[40] A. Ghosh, O. F. Mohammed, O. M. Bakr, *Acc. Chem. Res.* **2018**, *51*, 3094.
[41] M. A. Abbas, T.-Y. Kim, S. U. Lee, Y. S. Kang, J. H. Bang, *J. Am. Chem. Soc.* **2016**, *138*, 390.
[42] K. G. Stamplecoskie, P. V. Kamat, *J. Am. Chem. Soc.* **2014**, *136*, 11093.
[43] S. Takano, S. Hasegawa, M. Suyama, T. Tsukuda, *Acc. Chem. Res.* **2018**, *51*, 3074.
[44] M. S. Bootharaju, C. P. Joshi, M. R. Parida, O. F. Mohammed, O. M. Bakr, *Angew. Chem., Int. Ed.* **2016**, *55*, 922.
[45] M. Zhu, C. M. Aikens, F. J. Hollander, G. C. Schatz, R. Jin, *J. Am. Chem. Soc.* **2008**, *130*, 5883.
[46] X. Yu, Y. Sun, W. W. Xu, J. Fan, J. Gao, X. Jiang, Y. Su, J. Zhao, *Nanoscale Horiz.* **2022**, *7*, 1192.
[47] S. Maity, S. Kolay, S. Ghosh, S. Chakraborty, D. Bain, A. Patra, *J. Phys. Chem. Lett.* **2022**, *13*, 5581.
[48] M. Zhou, C. Yao, M. Y. Sfeir, T. Higaki, Z. Wu, R. Jin, *J. Phys. Chem. C* **2018**, *122*, 13435.
[49] S. V. Kilina, A. J. Neukirch, B. F. Habenicht, D. S. Kilin, O. V. Prezhdo, *Phys. Rev. Lett.* **2013**, *110*, 180404.
[50] Z. Zhou, J. Liu, R. Long, L. Li, L. Guo, O. V. Prezhdo, *J. Am. Chem. Soc.* **2017**, *139*, 6707.

© 2023 The Authors. Solar RRL published by Wiley-VCH GmbH

[51] D. E. Jiang, M. Kuhn, Q. Tang, F. Weigend, *J. Phys. Chem. Lett.* **2014**, *5*, 3286.
[52] J. Li, G. Zhan, Y. Yu, L. Zhang, *Nat. Comm.* **2016**, *7*, 11480.
[53] Y. Liu, T. Zhou, Y. Zheng, Z. He, C. Xiao, W. K. Pang, W. Tong, Y. Zou, B. Pan, Z. Guo, Y. Xie, *ACS Nano* **2017**, *11*, 8519.
[54] Y. Zheng, T. Zhou, X. Zhao, W. K. Pang, H. Gao, S. Li, Z. Zhou, H. Liu, Z. Guo, *Adv. Mater.* **2017**, *29*, 1700396.
[55] D. Mombrú, R. Faccio, Á. W. Mombrú, *Appl. Surf. Sci.* **2018**, *462*, 409.
[56] H. Yang, Y. Wang, H. Huang, L. Gell, L. Lehtovaara, S. Malola, H. Häkkinen, N. Zheng, *Nat. Comm.* **2013**, *4*, 2422.
[57] P. Zhang, Y. S. Ang, A. L. Garner, Á. Valfells, J. W. Luginsland, L. K. Ang, *J. Appl. Phys.* **2021**, *129*, 100902.
[58] J. Low, J. Yu, M. Jaroniec, S. Wageh, A. A. Al-Ghamdi, *Adv. Mater.* **2017**, *29*, 1601694.
[59] Y. Guo, H. Li, W. Ma, W. Shi, Y. Zhu, W. Choi, *Carbon Energy* **2020**, *2*, 308.
[60] G. Hu, Z. Wu, D.-e. Jiang, *J. Mater. Chem. A* **2018**, *6*, 7532.

© 2023 The Authors. Solar RRL published by Wiley-VCH GmbH